Three Dimensional Variable-Wavelength X-Ray Bragg Coherent Diffraction Imaging

W. Cha, A. Ulvestad, M. Allain, V. Chamard, R. Harder, S. J. Leake, J. Maser, P. H. Fuoss, and S. O. Hruszkewycz

Phys. Rev. Lett. **117**, 225501 — Published 23 November 2016

DOI: 10.1103/PhysRevLett.117.225501

Three dimensional variable-wavelength x-ray Bragg coherent diffraction imaging

W. Cha,[1] A. Ulvestad,[1] M. Allain,[2] V. Chamard,[2] R. Harder,[3] S. Leake,[4] J. Maser,[3] P. H. Fuoss,[1] and S. O. Hruszkewycz[1]

[1]*Materials Science Division, Argonne National Laboratory, Argonne, Illinois 60439, USA*
[2]*Aix-Marseille University, CNRS, Centrale Marseille, Institut Fresnel, UMR 7249, 13013 Marseille, France*
[3]*X-ray Science Division, Argonne National Laboratory, Argonne, Illinois 60439, USA*
[4]*ESRF – The European Synchrotron, CS 40220, 38043 Grenoble Cedex 9, France*

We present and demonstrate a formalism by which three dimensional (3D) Bragg x-ray coherent diffraction imaging (BCDI) can be implemented without moving the sample by scanning the energy of the incident x-ray beam. This capability is made possible by introducing a 3D Fourier transform that accounts for x-ray wavelength variability. We demonstrate the approach by inverting coherent Bragg diffraction patterns from a gold nanocrystal measured with an x-ray energy scan. Variable-wavelength BCDI will expand the breadth of feasible *in situ* 3D strain imaging experiments towards more diverse materials environments, especially where sample manipulation is difficult.

In materials, nanoscale distributions of strain and lattice distortions in crystals often dictate performance and properties [1], but are difficult to measure under realistic working conditions. Increasingly, Bragg coherent x-ray diffraction imaging (BCDI) is being utilized at synchrotron sources to address this challenge by non-destructively imaging nanoscale strain fields in crystalline materials in three dimensions (3D) using penetrating hard x-rays [2–7]. While these studies have shown great promise, the breadth of feasible 3D BCDI measurements could expand substantially if current experimental requirements such as sample rotation could be eliminated without sacrificing imaging capability.

In a Bragg diffraction experiment, the reciprocal space volume about a Bragg peak can be measured by finely scanning the wavelength of the incident beam (as opposed to its relative angle). Recent investigations have successfully mapped 3D Bragg peaks from crystals in this manner [8–10], but numerical phase retrieval and inversion of such measurements into 3D real space images have yet to be demonstrated. This capability would enable new strain imaging studies of materials in environments where sample manipulation is difficult and the details of nanoscale strain distribution and evolution remain elusive – for example during high-temperature crystal synthesis.

Here, we present a new variable-wavelength BCDI (vw-BCDI) approach that reconstructs a 3D image of strain and density of a crystalline nanoparticle from x-ray energy scan measurements, eliminating the need to rotate the sample. To reconstruct 3D images from this type of data, we introduce a new phase retrieval approach designed to handle x-ray wavelength (λ) variability in BCDI, and we demonstrate the method with experimental data.

Using BCDI, lattice distortions within a 3D nanocrystal can be determined from the coherent diffraction intensity distribution about a Bragg peak [4, 11]. A typical monochromatic BCDI experiment is shown schematically in Figure 1(a), which depicts a nanocrystal (ρ) that is illuminated with a coherent x-ray plane wave. The incident beam wavevector $\mathbf{k_i}$, exit beam wavevector $\mathbf{k_f}$, and nanocrystal are oriented such that the scattering vector $\mathbf{q} = \mathbf{k_f} - \mathbf{k_i}$ is in the vicinity of a Bragg reflection at the reciprocal lattice point $\mathbf{G_{HKL}}$. (Here, $|\mathbf{k}| = 2\pi/\lambda$.) The 3D intensity distribution surrounding the $\mathbf{G_{HKL}}$ Bragg peak from ρ is shown schematically in Figure 1(b) as a yellow isosurface. Near the Bragg condition, an area detector will measure a cut through this 3D intensity distribution along the plane normal to $\mathbf{k_f}$ that intersects $\mathbf{q}$ [13, 14]. Different slices can be measured by varying $\mathbf{Q} \equiv \mathbf{q} - \mathbf{G_{HKL}}$, the reciprocal space distance from the center of the area detector to the Bragg peak. As shown in Figure 1(a), in a typical single-wavelength experiment, $\mathbf{Q}$ changes over the course of a scan of the sample angle θ ($\pm \sim 0.5°$) while $|\mathbf{q}|$ remains fixed. Such an angle scan (rocking curve) is depicted in Figure 1(b) as a series of parallel grey planes slicing through the 3D Bragg peak intensity distribution. Thus, the Bragg 3D intensity distribution is recorded slice-by-slice. The oversampled intensity encodes the magnitude, but not the phase, of the 3D Fourier transform of the diffracting nanocrystal. To form a strain-sensitive image of the crystal, the set of measured slices that sample the 3D coherent intensity distribution are phased using reconstruction algorithms [12] that utilize forward and inverse discrete 3D Fourier transforms ($\mathcal{F}_{3D}$ and $\mathcal{F}_{3D}^{-1}$). However, because current BCDI reconstruction approaches apply 3D discrete Fourier transforms directly to the data set, measurements that utilize these algorithms need to be performed using a fixed x-ray wavelength.

An alternative method of measuring the 3D Bragg coherent diffraction intensity distribution is to vary the length of the scattering vector $\mathbf{q}$ while keeping the sample orientation fixed. This can be done by scanning the x-ray wavelength to change $|\mathbf{k}|$ and $|\mathbf{q}|$, thus varying $\mathbf{Q}$ as shown in Figure 1(c) [8–10]. As compared to the monochromatic case, such a scan will result in a different (though equally valid) set of slices with which to assemble the 3D Bragg intensity distribution (Figure 1(d)). However, such a data set is not suitable for discrete $\mathcal{F}_{3D}$-based BCDI reconstruction algorithms because $|\mathbf{k}|$ is not constant over the scan, and the scaling of reciprocal space in the detector changes at every measured slice. In the work featured here, this scaling changes by $\sim 4\%$ from the beginning to the end of the scan. Without accounting for the changing wavelength in the data set, this scaling builds in an artificial asymmetry in the fringe pattern about the Bragg peak. This situation is problematic and should not be ignored in BCDI

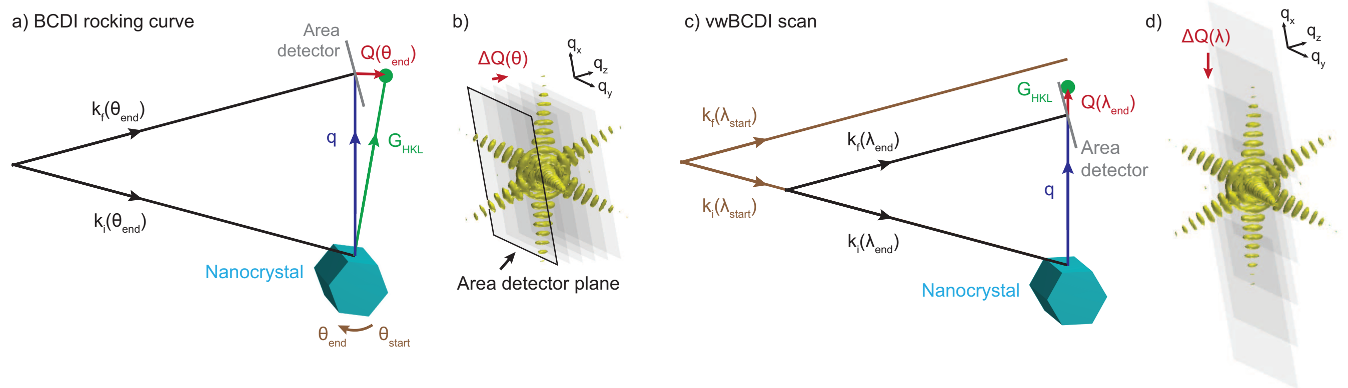

FIG. 1. This schematic depicts an isolated nanocrystal illuminated with a coherent beam and oriented such that the incident ($\mathbf{k_i}$) and exit ($\mathbf{k_f}$) beam wave vectors satisfy a Bragg condition for the HKL reflection (denoted by the reciprocal space vector $\mathbf{G_{HKL}}$). In such an experiment, the area detector accesses a 2D slice through the 3D reciprocal space intensity pattern. To measure various components of the 3D Bragg peak intensity distribution, the scattering condition $\mathbf{q} = \mathbf{k_f} - \mathbf{k_i}$ must be changed relative to $\mathbf{G_{HKL}}$, thus changing $\mathbf{Q} = \mathbf{q} - \mathbf{G_{HKL}}$. In a monochromatic experiment (a,b), this is done by changing the angle of the sample at a fixed $|\mathbf{q}|$. Alternatively, with a fixed sample position, the reciprocal space volume about the Bragg peak can be sampled by changing the wavelength of the x-ray beam (c,d).

because asymmetries of this order are also indicative of lattice imperfections in the crystal [15]. Interpolation of vwBCDI data onto a regular $\mathbf{q}$-space grid could be performed in order to utilize current algorithms. However, typical data interpolation approaches alter the observed Poisson photon counting statistics of the underlying intensity probability distribution function [16, 17] in weakly scattering regions that often convey high-spatial-resolution information.

Thus, reconstructing a 3D image from a vwBCDI measurement without interpolating intensity data requires a 3D Fourier transform operations that account for the changing wavelength on a slice-by-slice basis. A related concept has been successfully implemented in reconstructing broadband forward scattering coherent diffraction patterns [18], but did not deal with the reconstruction of a reciprocal space volume. To address this challenge for the Bragg geometry, we leverage the properties of the Fourier slice projection theorem [19, 20] and the relationship between spatial sampling and array size in a 2D discrete Fourier transform to define a slice-by-slice 3D Fourier transform appropriate for vwBCDI experiments. Our approach uses these concepts to perform simultaneous Fourier transformation and interpolation of each λ-dependent slice of the Bragg intensity distribution.

In a monochromatic BCDI scan of a Bragg peak in which $\mathbf{Q_j}$ varies over $j = 1 \cdots J$ two dimensional intensity measurements, the j^{th} 2D wave field at the detector is given by [13, 14, 21]: $\psi_j = \mathcal{F}\mathcal{R}\mathcal{Q}_j\rho$, in accordance with the Fourier slice projection theorem. In this expression, $\mathcal{Q}_j$ is a multiplicative linear phase gradient defined as $\mathcal{Q}_j = \exp[i\,\mathbf{r}\cdot\mathbf{Q_j}]$ that displacess the detector plane in reciprocal space away from Bragg peak maximum (the origin in $\mathbf{Q}$). $\mathcal{R}$ is a 3D$\rightarrow$2D projection along the direction of $\mathbf{k_f}$, $\mathcal{F}$ is a 2D Fourier transform, and ψ_j is the far field exit wave in the detector. The measured intensity is then given by $I_j = |\psi_j|^2$.

In calculating ψ_j, $\mathcal{F}$ is typically implemented with a discrete 2D Fourier transform of a pixelated image array. In this case, the relationship between the pixel size in real and reciprocal space in the plane is fixed [22]. In each dimension of the projection plane, the pixel size in real space is given by: $p_{\text{samp}} = \lambda D/(N_{\text{pix}}p_{\text{det}})$, where N_{pix} is the number of pixels along one dimension of the square array, p_{det} is the edge size of a square pixel in the area detector used in the measurement, and D is the sample-to-detector distance. In vwBCDI, we aim to maintain a constant p_{samp} for all $\psi(\lambda_j)$. To satisfy this condition when D and p_{det} are fixed, we can consider N_{pix} as a free parameter that varies with λ_j such that $\lambda_j/N_{\text{pix}}(\lambda_j)$ is constant. So long as N_{pix} for all λ_j is greater than the number of pixels in the physical detector (N_{det}), as in the case described here, then a direct comparison can be made between $\psi(\lambda_j)$ and experimental measurements.

Based on this principle, we introduce a modified 2D Fourier transform operator $\mathcal{F}_\lambda = S_\lambda^{-1}\mathcal{F}S_\lambda$ that maintains a constant p_{samp} by varying N_{pix}. Here, S_λ is an operator that pads the effective number of pixels in the array to an integer value $N_{\text{pix}}(\lambda_j)$ that scales with λ_j, enforcing the appropriate pixel sampling of each ψ_j via the discrete 2D Fourier transform. With this approach, the pixel size at the sample in the projection plane is set by experimental parameters. For a λ scan with a fixed step size of $\delta\lambda$, p_{samp} of the real space image is given by $(\delta\lambda)D/p_{\text{det}}$. Additionally, the integer range of N_{pix} is set by the largest λ in the scan: $N_{\text{pix}}^{\text{max}} = \lambda^{\text{max}}D/(p_{\text{samp}}p_{\text{det}})$. Therefore, invoking $\mathcal{S}_\lambda$ for a vwBCDI data set requires that the projection plane array be sampled with pixels of size p_{samp} and resized to $(N_{\text{pix}}^{\text{max}} + 1 - j)$ in both dimensions for a given λ_j. The $\mathcal{S}_\lambda^{-1}$ operator then resizes the array to a fixed size for all λ_j. In the case of $\mathcal{F}_\lambda$, this size is $N_{\text{det}} \times N_{\text{det}}$, where N_{det} is the number of physical pixels in the area detector.

Thus, the coherent wave field at the detector in a vwBCDI experiment is given by:

$$\psi_j = \mathcal{F}_{\lambda_j} \mathcal{R} \mathcal{Q}_j \rho. \tag{1}$$

To better illustrate the details of this calculation, we step through these operations. To begin, we define a conjugate pair of orthogonal spatial coordinates based on the orientation of $\mathbf{k_f}$: (r_x, r_y, r_z) and (q_x, q_y, q_z). The former is the basis for the real space vector $\mathbf{r}$ and the latter for the reciprocal space $\mathbf{q}$ and $\mathbf{Q}$. In real space, two directions r_x and r_y are normal to $\mathbf{k_f}$ and are aligned with the edges of a square area detector (outlined in black in Figure 1(b)). The third direction r_z is parallel to $\mathbf{k_f}$. q_x, q_y, and q_z are oriented parallel to their conjugate r-space counterparts.

A visual representation of the operators in Equation 1 is shown in Figure 2. First the crystal ρ is multiplied by a phase factor that depends on $\mathbf{Q}_j$ corresponding to a slice of the Bragg peak measured at a given λ_j. The complex 3D quantity $\mathcal{Q}_j \rho$ is then projected onto the (r_x, r_y) plane, sampled with real space pixels of size p_{samp}. By manipulating the number of pixels in the image array, the $\mathcal{F}_{\lambda_j}$ operator adjusts the scaling of ψ_j to correspond to λ_j. In this way, a series of diffraction patterns $\{\psi_1 \cdots \psi_J\}$ cutting through the Bragg intensity distribution can be generated for a scan of λ, as shown in Figure 2(g).

In order to enable phase retrieval and 3D image reconstruction, a conjugate inversion procedure must be introduced that converts the reciprocal space information in $\{\psi_1 \cdots \psi_J\}$ back to real space to recover ρ. Here, we take advantage of another feature of the Fourier slice projection theorem: that a 2D$\rightarrow$3D back-projection operation ($\mathcal{R}^\dagger$) can be used to re-assemble a 3D object from a series of 2D projections. We also utilize the fact that each ψ_j is offset from the Bragg peak by $\mathbf{Q_j}$. The component of $\mathbf{Q_j}$ along $\mathbf{k_f}$ encodes the spatial frequency along r_z for the projected structural information in the (r_x, r_y) plane contained in ψ_j. Thus, ρ can be expressed by inverting the operators in Equation 1 and summing the resulting back-projections.

$$\rho = \sum_{j=1}^{J} \mathcal{Q}_j^* \mathcal{R}^\dagger \mathcal{F}_{\lambda_j}^{-1} \psi_j. \tag{2}$$

In this expression, $\mathcal{F}_{\lambda_j}^{-1} = S_{\lambda_j}^{-1} \mathcal{F}^{-1} S_{\lambda_j}$, and $\mathcal{Q}_j^* = \exp[-i\,\mathbf{r} \cdot \mathbf{Q}_j]$ is the complex conjugate of $\mathcal{Q}_j$. In this expression, we use $\mathcal{S}_{\lambda_j}^{-1}$ to resize the real-space projection image to a size of $N_{\text{pix}}^{\max} \times N_{\text{pix}}^{\max}$.

Here, we step through the inverse operators used in Equation 2. Starting with a given ψ_j (amplitudes and phases known), $\mathcal{F}_{\lambda_j}^{-1}$ yields a projection of $\mathcal{Q}_j \rho$ on the (r_x, r_y) plane with pixel size p_{samp}. Next, the back-projection operator $\mathcal{R}^\dagger$ uniformly replicates this projection along r_z. Finally, $\mathcal{Q}_j^*$ imparts an oscillating phase profile that encodes the appropriate spatial frequency along r_z for this slice. $\mathcal{Q}_j^*$ can also encode phase gradients along r_x and r_y that account for displacement of the diffraction pattern from the central pixel of the detector at each slice. The quantity $\mathcal{Q}_j^* \mathcal{R}^\dagger \mathcal{F}_{\lambda_j}^{-1} \psi_j$ is calculated for all J diffraction patterns and summed. This process is visualized in Supplemental Figure S1 for the simulated nanocrystal featured in Figure 2a. It is shown that as the number of summed terms approach $J = 100$, the morphology and phase of the summation converge to ρ.

We note that $\mathcal{F}_\lambda$ and $\mathcal{F}_\lambda^{-1}$ generalize the forward and inverse Fourier transform operations that describe the reciprocal space 3D volume about a Bragg peak as measured by an area detector in a variable-wavelength measurement. Effectively, when S_λ and S_λ^{-1} are unity, the operations described in Equations 1 and 2 are equivalent to the traditionally used forward and inverse discrete 3D Fourier transforms. Thus, by integrating them into a phase retrieval algorithm, $\mathcal{F}_\lambda$ and $\mathcal{F}_\lambda^{-1}$ enable phase retrieval of vwBCDI data sets. Common phasing algorithms rely on minimizing the sum squared error between the measured intensity distribution and the far field exit wave of the reconstructed object: $\epsilon^2 = \parallel |\psi| - \sqrt{I} \parallel^2$. We adopt the same approach here, defining the sum squared error as $\epsilon^2 = \sum_j \parallel |\psi_j| - \sqrt{I_j} \parallel^2$. This error metric then becomes the basis for determining a gradient ∂_λ for phase retrieval, after Ref [21]:

$$\partial_\lambda = \sum_{j=1}^{J} \mathcal{Q}^* \mathcal{R}^\dagger \mathcal{F}_\lambda^{-1} \left(\psi_j - \sqrt{I_j} \frac{\psi_j}{|\psi_j|} \right). \tag{3}$$

Following Ref [12], we obtain the modulus constraint for vwBCDI: $P_m \rho = \rho - \frac{1}{2} \partial_\lambda$, that enforces consistency between the amplitudes of $\psi_{\{1 \cdots J\}}$ and the experimentally measured intensity patterns. The modulus constraint, when used in combination with an object-bounding support, is central to iterative BCDI phase retrieval algorithms such as Hybrid Input/Output (HIO) and Error Reduction (ER) [23]. (Pseudocode for ER/HIO implemented with ∂_λ is included in the Supplemental Information.) With ∂_λ, these reconstruction algorithms can be applied to experimental data.

To demonstrate the phase retrieval approach introduced above, vwBCDI measurements were performed on a sub-micron-sized Au nanocrystal [24]. Measurements were performed with a mirror-focused coherent x-ray beam at the Sector 34-ID-C beamline at the Advanced Photon Source. The 111 Bragg condition was satisfied at 9 keV (far from any Au absorption edges) with a symmetric diffraction geometry (Bragg angle of $\theta_{Br} = 17°$). In this experiment, $D = 0.62$ m, $p_{\text{det}} = 55\ \mu$m, and $N_{\text{det}} = 256$. The scattering geometry was fixed, and the energy of the incident beam was scanned from 8.85 to 9.15 keV in 6 eV increments (corresponding to a $\delta\lambda \sim 8.9 \times 10^{-4}$ Å and $\lambda^{\min} = 1.378$ Å). The synchrotron undulator gap was adjusted at every energy step in order to provide nearly constant flux at all λ_j [10]. Under these conditions, $p_{\text{samp}} = 1.0$ nm and $N_{\text{pix}}^{\max} = 1576$ [25]. For comparison, data were also collected at 9 keV with a rocking curve $(\theta_{Br} \pm 0.35°)$ in $0.01°$ angular increments.

HIO and ER were used with the ∂_λ gradient to reconstruct a 3D image of the Au crystal from the vwBCDI data, and

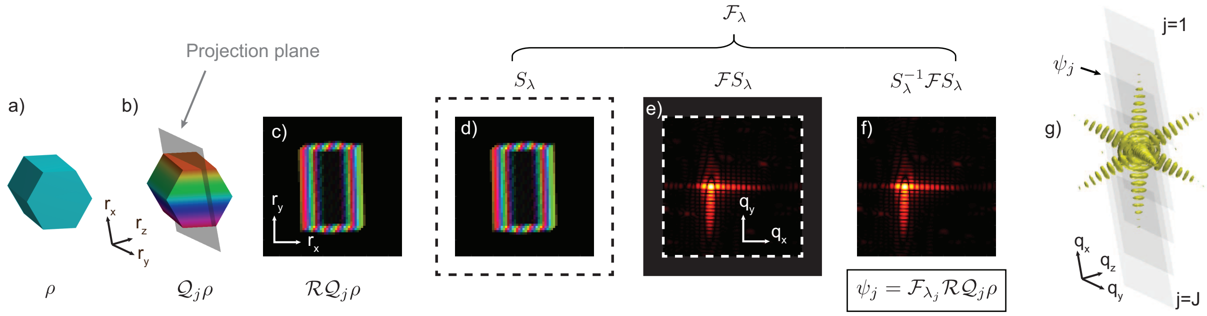

FIG. 2. Schematic of a slice-by-slice calculation of vwBCDI diffraction patterns. (a) The nanocrystal ρ is multiplied by a phase factor, resulting (b) in $\mathcal{Q}_j\rho$. (c) The 3D quantity $\mathcal{Q}_j\rho$ at a given λ is projected onto the (r_x, r_y) plane via the projection operator $\mathcal{R}$. In order to properly scale the diffraction pattern for this λ, the operator $\mathcal{F}_\lambda$ is invoked, defined as $S_\lambda^{-1}\mathcal{F}S_\lambda$, shown in (d-f). (d) S_λ changes the number of pixels in the image to $N_{\text{pix}}(\lambda_j)$ by padding with zeros. (e) A 2D Fourier transform $\mathcal{F}$ of the padded projection array is applied. (f) S_λ^{-1} re-sizes the resulting array back to a fixed pixel size, in this case $N_{\text{det}} \times N_{\text{det}}$. (g) In this manner, each slice (gray plane) through a 3D Bragg peak intensity distribution (yellow isosurface) is calculated resulting in the set $\{\psi_1 \cdots \psi_J\}$ that mimics a vwBCDI measurement. The inverse process of reconstructing ρ from $\{\psi_1 \cdots \psi_J\}$ involves inverting the above operators (including $\mathcal{F}_\lambda^{-1}$), and is demonstrated graphically in Supplementary Figure S1.

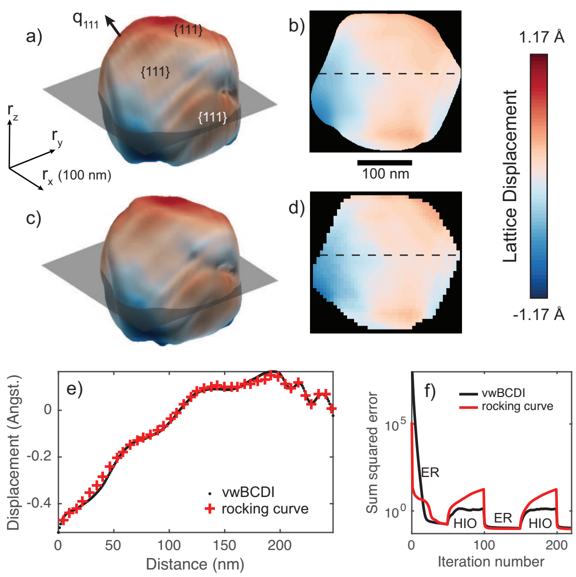

FIG. 3. (a) A density isosurface of an Au nanocrystal reconstructed using vwBCDI. Coloring corresponds to near-surface lattice displacements. {111} facets are labeled, and the arrow q_{111} indicates the scattering vector direction of the measured Bragg peak. (b) The lattice displacement within the nanocrystal along the gray plane in (a). Corresponding images of the same crystal reconstructed from rocking-curve based BCDI data (c, d). (e) Comparison of lattice displacement line-outs along the dotted lines in (b) and (d). Error metrics from vwBCDI and standard rocking curve phase retrieval are shown in (e).

standard $\mathcal{F}_{3D}$-based HIO and ER were applied to the rocking curve data. Both data sets were successfully phased with comparable rates of convergence, and the resulting reconstructions are shown in Figure 3. A 3D isosurface of the electron density of both reconstructions is featured, showing regions of higher lattice displacement especially near the edges and corners of {111} facets, as has been observed previously in gold nanoparticles prepared by thermal dewetting of films [26]. Direct comparisons of the images is difficult because the measured reciprocal space volumes and sampling of the Bragg peak from the energy and rocking scans are inherently different, leading to expected differences in the pixelation and resolution of features in the reconstructions. Nonetheless, the lattice displacements traced along equivalent lines of both reconstructions agree well (Figure 3(e)). We note that for larger crystals, refraction effects can become significant and should be accounted for [27].

The good agreement between the two reconstruction methods demonstrates that vwBCDI preserves the strain-sensitive 3D imaging capability of current rocking-curve-based BCDI methods *without* requiring any sample motion. This capability will greatly simplify certain *in-situ* strain measurements in environments that are difficult to accurately rotate about a precise center of rotation or that are otherwise cumbersome. The current formalism does not incorporate the energy dependence of the scattering factor. Thus, vwBCDI scans should be performed far away from absorption edges of the elements in the sample. However, enabling element-sensitive vwBCDI may be feasible with near-edge energy scanning if additional resonant scattering effects are incorporated into the phase retrieval algorithm.

Development of variable x-ray wavelength transforms was supported by the U.S. Department of Energy, Office of Science, Basic Energy Sciences, Materials Sciences and Engineering Division. Creation of back-projection operators for Bragg diffraction was partially funded by the French ANR under project number ANR-11-BS10-0005. Sample preparation was supported by EPSRC Grant No. EP/D052939/1. Use of the Advanced Photon Source was supported by the U. S. Department of Energy, Office of Science, Office of Basic Energy Sciences, under Contract No. DE-AC02-06CH11357. The authors gratefully acknowledge the APS-XSD Optics Group for help with sample preparation.

[1] J. Li, Z. Shan, and E. Ma, Mrs Bulletin **39**, 108 (2014).
[2] I. K. Robinson, I. Vartanyants, G. Williams, M. Pfeifer, and J. Pitney, Physical Review Letters **87**, 195505 (2001).
[3] M. A. Pfeifer, G. J. Williams, I. A. Vartanyants, R. Harder, and I. K. Robinson, Nature **442**, 63 (2006).
[4] I. Robinson and R. Harder, Nature Materials **8**, 291 (2009).
[5] W. Cha, et al., Nature Materials, **12,** 729 (2013).
[6] A. Ulvestad, A. Singer, J. N. Clark, H. M. Cho, J. W. Kim, R. Harder, J. Maser, Y. S. Meng, and O. G. Shpyrko, Science **348**, 1344 (2015).
[7] J. N. Clark, L. Beitra, G. Xiong, D. M. Fritz, H. T. Lemke, D. Zhu, M. Chollet, G. J. Williams, M. M. Messerschmidt, B. Abbey, et al., Proceedings Of The National Academy Of Sciences Of The United States Of America **112**, 7444 (2015).
[8] W. Cha, W. Liu, R. Harder, R. Xu, P. H. Fuoss, and S. O. Hruszkewycz, Journal of Synchrotron Radiation **23**, 1241 (2016).
[9] T. W. Cornelius, A. Davydok, V. L. R. Jacques, R. Grifone, T. Schulli, M. I. Richard, G. Beutier, M. Verdier, T. H. Metzger, U. Pietsch, et al., Journal of Synchrotron Radiation **19**, 688 (2012).
[10] T. W. Cornelius, D. Carbone, V. L. R. Jacques, T. U. Schülli, and T. H. Metzger, Journal of Synchrotron Radiation **18**, 413 (2011).
[11] J. Stangl, C. Mocuta, V. Chamard, D. Carbone, *Nanobeam x-ray scattering: Probing matter at the nanoscale*, Wiley-VCH (2013).
[12] S. Marchesini, Review Of Scientific Instruments **78**, 011301 (2007).
[13] S. O. Hruszkewycz, M. V. Holt, M. Allain, V. Chamard, S. M. Polvino, C. E. Murray, and P. H. Fuoss, Optics Letters **40**, 3241 (2015).
[14] I. Vartanyants and I. Robinson, Journal Of Physics-Condensed Matter **13**, 10593 (2001).
[15] M. Dupraz, G. Beutier, D. Rodney, D. Mordehai, and M. Verdier, Journal of Applied Crystallography, **48,** 621 (2015).
[16] P. Godard, M. Allain, V. Chamard, and J. Rodenburg Optics Express **20**, 25914 (2012).
[17] P. Thibault and M. Guizar-Sicairos, New Journal of Physics, **14,** 063004 (2011).
[18] B. Abbey, et al., Nature Photonics, **5,** 420 (2011).
[19] A. C. Kak and M. Slaney, *Principles of Computerized Tomographic Imaging*, IEEE Press (1988).
[20] F. Natterer and F. Wübbeling, *Mathematical Methods in Image Reconstruction,* SIAM, Philadelphia, (2001).
[21] S. O. Hruszkewycz, M. Allain, M. V. Holt, C. E. Murray, J. R. Holt, P. H. Fuoss, V. and Chamard, arXiv:1506:01262.
[22] J. W. Goodman, *Introduction to Fourier Optics*, 3rd ed., Roberts & Company (2004).
[23] J. Fienup, Applied Optics **21**, 2758 (1982).
[24] Samples were prepared by sputtering a layer of gold onto a single crystal silicon substrate with a gradient of thickness ranging from 0-1000 nm. To form nanoparticles via thermal dewetting of the film, the coated substrate was annealed in an inert atmosphere with the following heat treatment: 1100°C for 6 hours, 1000°C for 2 hours, 900°C for 2 hours. The dewetting process resulted in gold nanocrystals of various diameters that were rigidly adhered to the silicon substrate.
[25] We note that the formalism presented above assumes data were collected linearly in λ. Due to instrumental considerations, our measurement was performed with a fixed energy step that introduced variability in $\delta\lambda$ of a few percent over the scan. Nevertheless, the measurement approximated a linear λ scan sufficiently so as to demonstrate the principle here.
[26] M. Watari, R. A. McKendry, M. Vogtli, G. Aeppli, Y-. A. Soh, X. Shi, G. Xiong, X. Huang, R. Harder, I. K. Robinson. Nature Materials, **10,** 862 (2011).
[27] R. Harder, M. A. Pfeifer, G. J. Williams, I. A. Vartaniants, I. K. Robinson. Physical Review B, **76,** 115425 (2007).